Light-Activated Gigahertz Ferroelectric Domain Dynamics

Hirofumi Akamatsu,[1] Yakun Yuan,[1] Vladimir A. Stoica,[1,2] Greg Stone,[1] Tiannan Yang,[1] Zijian Hong,[1] Shiming Lei,[1] Yi Zhu,[2] Ryan C. Haislmaier,[1] John W. Freeland,[2] Long-Qing Chen,[1] Haidan Wen,[2] and Venkatraman Gopalan[1,3,*]

[1]*Materials Research Institute and Department of Materials Science and Engineering, Pennsylvania State University, MSC Building, University Park, Pennsylvania 16802, USA*

[2]*Advanced Photon Source, Argonne National Laboratory, Argonne, Illinois 60439, USA*

[3]*Department of Physics, Pennsylvania State University, University Park, Pennsylvania 16802, USA*

(Received 29 July 2017; published 26 February 2018)

Using time- and spatially resolved hard x-ray diffraction microscopy, the striking structural and electrical dynamics upon optical excitation of a single crystal of $BaTiO_3$ are simultaneously captured on subnanoseconds and nanoscale within individual ferroelectric domains and across walls. A large emergent photoinduced electric field of up to 20×10^6 V/m is discovered in a surface layer of the crystal, which then drives polarization and lattice dynamics that are dramatically distinct in a surface layer versus bulk regions. A dynamical phase-field modeling method is developed that reveals the microscopic origin of these dynamics, leading to gigahertz polarization and elastic waves traveling in the crystal with sonic speeds and spatially varying frequencies. The advances in spatiotemporal imaging and dynamical modeling tools open up opportunities for disentangling ultrafast processes in complex mesoscale structures such as ferroelectric domains.

DOI: 10.1103/PhysRevLett.120.096101

The fast-paced improvements in ultrafast radiation, from x-ray and ultraviolet to terahertz frequencies, are enabling a simultaneous probe of electron, phonon, and spin dynamics on picosecond-to-nanosecond time scales, as well as submicrometer length scales [1–10]. There is emerging recognition now that ultrafast dynamics and the appearance of new phenomena depend not only on the intrinsic properties of the compound but also, strongly, on mesoscale structures such as surfaces, domains, walls, interfaces, and defects that govern the coupling between various order parameters [11]. Previous experimental studies on the dynamics of ferroelectrics largely fall into two categories: high spatial resolution (down to nanometer or atomic scale) but slow temporal resolution (millisecond and above) [12–20], or high temporal resolution (down to 100 fs), but low spatial resolution (tens of microns and above) [21–24]. Although the latter provides structural information on the atomistic scales by ultrafast x-ray diffraction, the mesoscale dynamics of domain evolution is spatially averaged [10,24–27]. A key challenge in disentangling these results is that the former is not suited for discovering transient phenomena on ultrafast time scales, while in the latter case, the intricate details of the local dynamics can be lost via spatially averaged probes.

Here, we report on simultaneous high-resolution spatial and temporal mapping of domains and domain walls in a multidomain ferroelectric bulk single crystal of $BaTiO_3$ using ultrafast x-ray and optical pulses. Analysis of the spatiotemporal structural dynamics reveals an emergent electric field around 20 MV/m induced by irradiating the surface with 400 nm femtosecond optical pulses, resulting in gigahertz polarization and lattice waves. Stroboscopic probing by x-ray pulses that are ≈100 ps in duration and ≈350 nm in size [28] yields atomistic structural dynamics within individual domains and across domain walls. Low frequency gigahertz acoustic pulses excited within domains are spatially tracked in different domain orientations and across domain walls. A dynamical phase-field modeling (DPFM) method is developed to show that this large surface field tilts the polarization of the *a* domain out of plane, and sets up a gigahertz wave which expands the *c* domains and shrinks the *a* domains in a damped oscillatory motion on picosecond-to-nanosecond time scales [24]. Excellent agreement is observed between the modeling and the experiments. The combination of theory and experiments reveals subsonic domain wall motion at speeds of 2.5 m/s within the first nanosecond after optical excitation, approaching the ultimate speed limit of wall motion of a few unit cells on subnanosecond time scales [29]. The spatial dependence of the surface and subsurface domain dynamics uncovered by this Letter highlights the value of such spatiotemporal studies combined with DPFM in understanding ultrafast phenomena in complex mesoscale domain structures.

The $BaTiO_3$ single crystal is one of the earliest ferroelectrics discovered [30–32]. At room temperature, it exhibits a tetragonal structure with a point group symmetry of 4 *mm*. The crystal used in this Letter contains both *a* domains, with polarization parallel to the crystal surface (depicted in green), and *c* domains, with polarization normal to the crystal surface (depicted in yellow), as illustrated in Fig. 1(a). The *a* domains and *c* domains

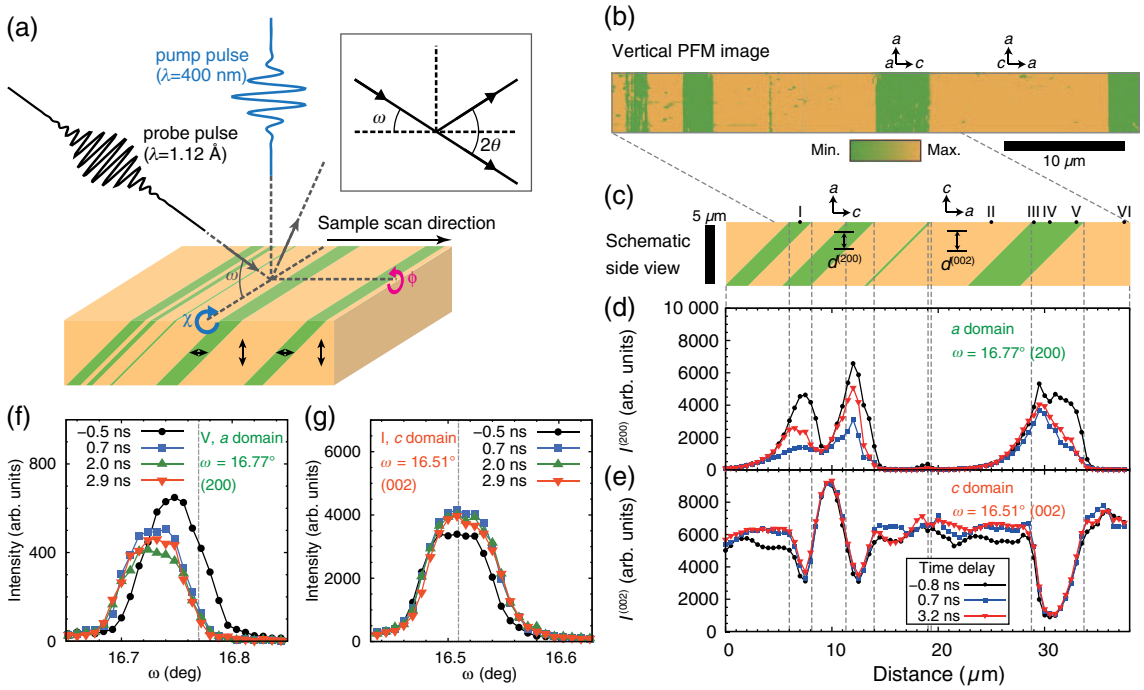

FIG. 1. (a) Schematic illustration of a spatially resolved pump-probe experiment and domain configuration of $BaTiO_3$ single crystal sample. (Inset) The incident plane. The tilting angles of domains χ and ϕ are also shown. a and c domains are depicted in green (polarization in the crystal plane depicted by double-headed black arrows) and orange (polarization perpendicular to the surface), respectively. (b) Vertical piezoresponse force microscopy image on the top surface. (c) Schematic domain wall structures derived from spatial mapping of (200) and (002) reflection intensities at $\omega = 16.77°$ and 16.51° for various time delays, shown in (d) and (e), respectively. The ω scan profiles for various time delays around (f) (200) and (g) (002) reflections at the locations V and I, respectively, labeled in (c).

are separated by 90° domain walls and are clearly revealed by piezoresponse force microscopy image of the crystal surface [Fig. 1(b)]. Along the depth of the crystal, the domain walls are aligned at 45° with respect to the crystal surface. The acquisition of spatiotemporal x-ray diffraction (XRD) maps of these domains was performed on the 7ID-C beam line at the Advanced Photon Source at the Argonne National Laboratory, and it is depicted in Fig. 1(a) (see details in the Supplemental Material, Sec. I [33]). Figure 1(c) schematically depicts the a- and c-domain depth profile, and their respective lattice spacing $d^{(200)}$ and $d^{(002)}$, within the crystal, and the corresponding x-ray probe locations (marked I–VI). In the area of interest, a fractional volume of the a domains is ≈30%. An optical pump pulse with 400 nm in wavelength was derived by doubling the output of a Ti:sapphire laser, and it was passed through a fused silica rod to lengthen the pulse duration for avoiding sample surface damage. This pump laser pulse with a pulse duration of 330–560 fs then was focused to a 50 μm diameter on the sample with a penetration depth of 30 μm. Given the penetration depth of x-ray pulses with a photon energy of 11 keV (≈10 μm) [see Fig. S1(c) of the Supplemental Material, Sec. II [33]], XRD intensity was observed from both the surface and the underlying subsurface domains at many locations across the sample, shown as well-separated diffraction peaks recorded on the area detector. The surface and subsurface domain type, a or c, can be determined from the corresponding XRD intensity from each domain [Figs. 1(d) and 1(e)]. Observed changes in the XRD intensity arise from both crystal distortions and rotations. To separate the two effects, rocking curves at different probe delay times were collected in Figs. 1(f) and 1(g). Both the line scans at different pump-probe time delays [Figs. 1(d) and 1(e)] and the rocking curves [Figs. 1(f) and 1(g)] form a complete spatiotemporal data set for this crystal.

We focus our attention on six spatial locations (I–VI) across different domain walls for the analyses of the spatiotemporal x-ray data; these locations are indicated in Fig. 2(a), and the relevant d spacing is indicated in the schematic diagram of Fig. 2(b). Of these, locations labeled I, III, IV, and V are surface a domains, and locations II and VI are surface c domains. For each of the four above-listed a-domain locations, there is a subsurface c domain underneath it, and similarly for both c-domain imaged locations, there is a subsurface a domain. Figure 2(c) plots the temporal diffraction intensity changes at a fixed diffraction angle for the surface a domain as well as the subsurface c domain at position I. Clear oscillations are observed with nanosecond periodicities that indicate gigahertz frequencies. By performing the $\omega - 2\theta$ scans at each time delay for a number of spatial locations, one can extract the changes in the out-of-plane lattice parameter $\Delta d/d_0^{(200)}$ and $\Delta d/d_0^{(002)}$,

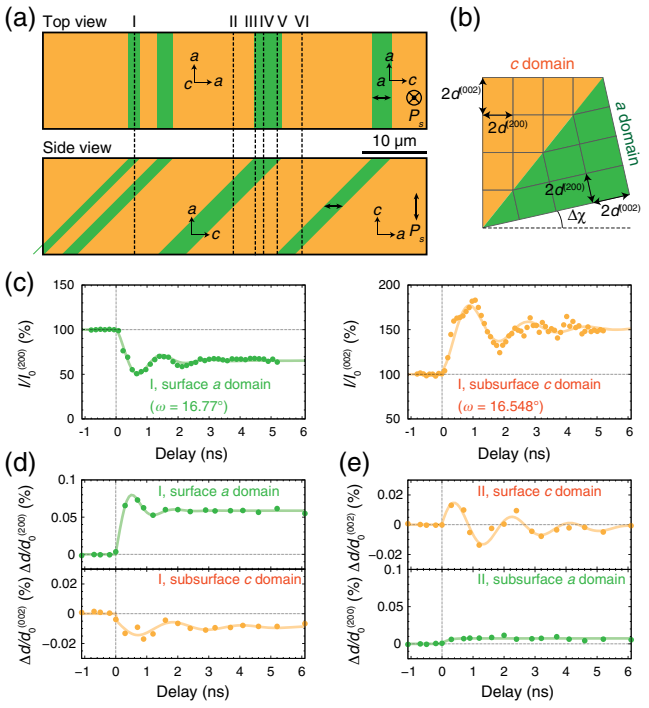

FIG. 2. (a) Locations I–VI at which time-delay dependent XRD measurements were performed. (b) Lattice spacings of (200) and (002) planes for a and c domains are illustrated. The difference between rotation angles χ for a and c domains, $\Delta\chi$, is depicted. (c) Time-delay dependence of (200) ($\omega = 16.77°$) and (002) ($\omega = 16.548°$) intensities relative to those before $t = 0$, $I/I_0^{(200)}$, and $I/I_0^{(002)}$, respectively, at location I, taken with a pump fluence of 66.2 mJ/cm^2. The (200) and (002) lattice-spacing change for a and c domains from those before $t = 0$, $\Delta d/d_0^{(200)}$, and $\Delta d/d_0^{(002)}$, respectively, as a function of time delay at the locations (d) I and (e) II. The solid lines in (c)–(e) are fits made by a damped oscillator model.

as plotted in Figs. 2(d) and 2(e). The green curves are the surface a domains at location I, and the subsurface a domains at location II. The orange curves are the subsurface c domains at location I, and surface c domains at location II. Similar data were collected for spatial locations III–VI (see Fig. S2 of the Supplemental Material, Sec. III [33]).

We first make some general observations from the spatiotemporal domain dynamics: There are two distinct sets of structural dynamics, i.e., surface and subsurface. We estimate the upper bound for the surface region to be confined to a depth of $\lesssim 700$ nm, as indicated by the data taken at location V, where the subsurface c domain buried $\approx$700 nm underneath exhibits lattice dynamics behavior characteristic of the subsurface region (see Fig. S2 of the Supplemental Material, Sec. III [33]). After photoexcitation, the out-of-plane lattice spacing increases within the first $\approx$100–150 ps for both the surface a domain ($\Delta d/d_0^{(200)} \approx 0.06\%$–$0.08\%$), and the surface c domains ($\Delta d/d_0^{(002)} \approx 0.02\%$). By contrast, the out-of-plane lattice spacing slightly increases for the subsurface a domain ($\Delta d/d_0^{(200)} \approx 0.01\%$), and it decreases for the subsurface c domain ($\Delta d/d_0^{(002)} \approx -0.02\%$) within the same time period. Thereafter, oscillations about this new lattice spacing with a damping time constant of a few nanoseconds are observed, which decay back to zero (not shown) by the time the subsequent optical pulse arrives at the sample ($\sim$1 ms).

To quantitatively understand the dynamics, we fit the time-dependent $\Delta d/d_0^{(200)}$ and $\Delta d/d_0^{(002)}$ data, Figs. 2(d) and 2(e), after time zero using the following damped acoustic oscillator model: $\Delta d/d_0(t) = A + B\exp(-\gamma t)\times \cos[2\pi\nu(t-\phi)]$. The fitting parameters at all of the locations are given in Tables S1 and S2 of the Supplemental Material, Sec. IV [33]. Typically, the oscillation frequency falls between $\nu \approx 0.2$–0.7 GHz, with a damping rate of $\gamma \approx 0.03$–5 ns^{-1}. The 90° domain walls intersect the surface at 45° and create wedgelike surface domains viewed from the cross section. By plotting twice the domain thickness l of the wedge-shaped surface a and c domains versus the ν^{-1} of the gigahertz waves at that location on the wedge (See Fig. S4 of the Supplemental Material, Sec. IV [33]), we observe an approximate linear trend of increasing inverse oscillation frequency ν^{-1} with an increasing wedge thickness l. The slope $2l/\nu^{-1} \approx 5.9 \times 10^3$ m/s obtained from Fig. S4 of the Supplemental Material [33] is strikingly close to the reported speed of sound in $BaTiO_3$ of $\approx 5.2 \times 10^3$ m/s [43]. This suggests that vertical oscillations of the surface reflect standing elastic waves of sonic frequency between the surface and the subsurface domain walls. Through DPFM, we will demonstrate shortly that these oscillations arise from polarization dynamics.

We focus next on the differences in structural dynamics between surface and subsurface regions, and their underlying mechanism. One notes from Figs. 2(d) and 2(e) that the c-lattice parameter initially increases for the surface c domains [see Fig. 2(e), location II], which at first glance seems to be contrary to a pure thermal effect [44]. We also carefully considered whether such a lattice parameter change could arise due to local optical heating of a region that is clamped by the surrounding unheated region; using DPFM as described further on, we clearly rule out this possibility (see the Supplemental Material, Sec. VII [33]). Furthermore, the maximum expected temperature change, ΔT, due to the linear absorption of an optical pump is small, < 0.5 °C [see Fig. S1(d) of the Supplemental Material, Sec. II [33]]. By estimating the nonlinear absorption from Ref. [45], the overall temperature change expected for our experimental pump fluence of 66.2 mJ/cm^2 is $\Delta T \sim 1$ °C $-$ 10 °C; a nonlinear coefficient of 2.3 cm/GW gives rise to a temperature change of $\sim$6° C, which gives the best DPFM fit to experiments, as described next. Lattice parameter changes caused only by thermal

expansion are a half order of magnitude smaller than the changes in the surface lattice parameters observed experimentally. Finally, the pump-fluence dependence of domain dynamics shown in the Supplemental Material, Sec. V [33] clearly indicates that the time constant decreases at higher pump fluences. Since the time constant for thermal diffusion should be independent of the temperature change and hence the pump fluence, this suggests that the observed structural changes are not purely driven by thermal diffusion. For all of these reasons, we need to consider additional nonthermal effects.

To understand the complex dynamics on the ultrafast time scale revealed by the experiments above, we have developed a DPFM approach. The dynamic response of the polarization $\mathbf{P}(\mathbf{r})$ is described using the modified time-dependent Ginzburg-Landau equation with an additional term in the second derivative of $\mathbf{P}$ with respect to time, accounting for intrinsic oscillation of the polarization, written as

$$\mu\frac{\delta^2\mathbf{P}}{\delta t^2}+\gamma\frac{\delta\mathbf{P}}{\delta t}+\frac{\delta F}{\delta\mathbf{P}}=0, \tag{1}$$

where μ and γ are kinetic coefficients related to domain wall mobility. The equation follows the form of a nonlinear Klein-Gordon equation previously derived with a Hamiltonian description of a ferroelectric system [46,47]. It is numerically solved using a semi-implicit Fourier spectral method. $F=F_{\text{Landau}}+F_{\text{gradient}}+F_{\text{electric}}+F_{\text{elastic}}$ is the total free energy of the ferroelectric $BaTiO_3$, where F_{Landau}, F_{gradient}, F_{electric}, and F_{elastic} are the ferroelectric Landau free energy, the ferroelectric gradient energy, the electrostatic energy, and the elastic energy, respectively, with formulations given in Refs. [48,49]. The details of the DPFM modeling are described in the Supplemental Material, Sec. VI [33].

DPFM was performed for a $BaTiO_3$ crystal with periodic boundary conditions, as shown in Fig. 3(a). A pure temperature change of $\Delta T\sim 6\,^{\circ}\text{C}$ results in excellent agreement with the experimentally observed lattice distortions in the subsurface region indicated in Fig. 3(b). However, a pure thermal effect is insufficient to explain the experimentally observed surface structural dynamics within the $\lesssim 700$ nm depth near the surface. Motivated by past reports of a possible surface layer [50–56], we explored an electric field of $\approx 2\times 10^7$ V/m in DPFM, parallel to the polarization direction in the c domains and perpendicular to the polarization direction in the a domains. When this field is combined with a temperature change of $\Delta T\approx 6\,^{\circ}\text{C}$, DPFM predicts gigahertz oscillations that are in outstanding agreement with experiments, as seen in Fig. 3(b), and thus provides insight into their origin. The impulsive photoinduced electric field of 20 MV/m expands c domains and shrinks the a domains by activating domain wall motions. As a result, the c domain grows by $\approx$4 unit cells or $\approx$1.5 nm within 0.6 ns, leading to a

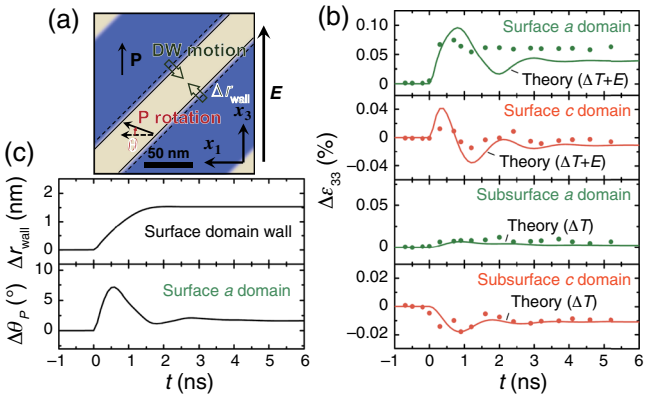

FIG. 3. (a) The a- and c-domain configurations used in DPFM. The displacement of the 90° domain walls (DWs) Δr_{wall} and a rotation of the polarization (P) inside a domain towards the out-of-plane direction ($\Delta\theta$) are illustrated as the effect of the field in the surface layer. (b) The experimental and theoretical $\Delta\epsilon_{33}$, as a function of time, in the surface and subsurface domains. (c) Δr_{wall} and $\Delta\theta$, as a function of time, in the crystal surface layer under the photoinduced electric field.

subsonic domain growth speed of 2.5 m/s within the first nanosecond after excitation [Fig. 3(c)]. In addition, the photoinduced surface field induces a polarization normal to the surface and tilts the polarization of the a domain from the in-plane to the out-of-plane direction by up to 7.5° over 0.5 ns, which leads to an increase in the out-of-plane lattice spacing [Fig. 3(c)]. The slight expansion of the c domains and the tilting of the polarization in the a domains lead to polarization and lattice waves that propagate at the speed of sound and exhibit a damped oscillatory behavior with gigahertz frequencies. The outstanding agreement between experiments and DPFM for both surface and subsurface lattice behavior, each for both a and c domains [Fig. 3(a)], enables these insights. Surface layer electric field geometries in DPFM other than the out-of-plane field discussed above gave poor agreement with the experiments (see Fig. S8 of the Supplemental Material, Sec. VIII [33]), thus ruling them out. The slight dynamic expansion of the c domain was confirmed using optical pump, optical second harmonic generation (SHG) probing [see the Supplemental Material, Sec. IX [33]]. SHG polarimetry shows a c-domain fraction of ≈54.8% before 400 nm optical pumping and ≈57.7%, 2 ns after pumping.

In conclusion, spatiotemporal imaging of the structural and polarization dynamics of ferroelectric domains using ultrafast XRD microscopy, combined with a newly developed DPFM code, reveals a large emergent photoinduced surface layer electric field of 20 MV/m in the surface region ($\lesssim 700$ nm) of $BaTiO_3$ single crystals that is created by an optical pump pulse. This temporal electric field sets up polarization dynamics that involves impulsively tilting the polarization of a domains out of the plane of the crystal and expanding the c domains at subsonic speeds, which leads to gigahertz polarization and elastic waves that are

directly imaged. The excellent agreement between DPFM and experiments helps reveal many of the subtleties of the emergent ultrafast phenomena observed in this Letter. In contrast to spatially averaged ultrafast studies, spatiotemporally resolved experiments such as those discussed in this Letter and in other works under development [3,6,14,57], combined with new theoretical tools such as DPFM, will become increasingly critical towards a fundamental understanding of ultrafast emergent phenomena on the mesoscale.

H. A., Y. Y., V. A. S., H. W., J. W. F., and V. G. were supported by the U.S. Department of Energy, Office of Science, Office of Basic Energy Sciences, under Grant No. DE-SC0012375, for the ultrafast XRD microscopy and ultrafast optical pump SHG probe work. The use of the Advanced Photon Source was supported by the U.S. Department of Energy, Office of Science, Office of Basic Energy Sciences under Contract No. DE-AC02-06CH11357. G. S., S. L., R. C. H., and Z. H. were supported by NSF Grant No. DMR-1420620 for the XRD data analysis, PFM measurements, UV-visible absorption measurements, and DPFM. T. Y. and L.-Q. C. acknowledge the support of the NSF under Grant No. DMR-1410714 for the DPFM work. We would like to thank Professor Aaron Lindenberg, Burak Guzelturk, Dr. Jianjun Wang, and Dr. Fei Xue for the helpful discussions and suggestions on DPFM.

*vxg8@psu.edu

[1] J. Zhang and R. Averitt, Annu. Rev. Mater. Res. **44**, 19 (2014).
[2] F. Chen, J. Goodfellow, S. Liu, I. Grinberg, M. C. Hoffmann, A. R. Damodaran, Y. Zhu, P. Zalden, X. Zhang, I. Takeuchi *et al.*, Adv. Mater. **27**, 6371 (2015).
[3] E. Szilagyi, J. S. Wittenberg, T. A. Miller, K. Lutker, F. Quirin, H. Lemke, D. Zhu, M. Chollet, J. Robinson, H. Wen *et al.*, Nat. Commun. **6**, 6577 (2015).
[4] W. Hu, S. Kaiser, D. Nicoletti, C. R. Hunt, I. Gierz, M. C. Hoffmann, M. Le Tacon, T. Loew, B. Keimer, and A. Cavalleri, Nat. Mater. **13**, 705 (2014).
[5] B. Zhang, D. F. Gardner, M. D. Seaberg, E. R. Shanblatt, H. C. Kapteyn, M. M. Murnane, and D. E. Adams, Ultramicroscopy **158**, 98 (2015).
[6] M. D. Seaberg, B. Zhang, D. F. Gardner, E. R. Shanblatt, M. M. Murnane, H. C. Kapteyn, and D. E. Adams, Optica **1**, 39 (2014).
[7] M. Matsubara, A. Schroer, A. Schmehl, A. Melville, C. Becher, M. Trujillo-Martinez, D. G. Schlom, J. Mannhart, J. Kroha, and M. Fiebig, Nat. Commun. **6**, 6724 (2015).
[8] H. Wen, L. Guo, E. Barnes, J. H. Lee, D. A. Walko, R. D. Schaller, J. A. Moyer, R. Misra, Y. Li, E. M. Dufresne *et al.*, Phys. Rev. B **88**, 165424 (2013).
[9] H. Wen, P. Chen, M. P. Cosgriff, D. A. Walko, J. H. Lee, C. Adamo, R. D. Schaller, J. F. Ihlefeld, E. M. Dufresne, D. G. Schlom *et al.*, Phys. Rev. Lett. **110**, 037601 (2013).
[10] D. Daranciang, M. J. Highland, H. Wen, S. M. Young, N. C. Brandt, H. Y. Hwang, M. Vattilana, M. Nicoul, F. Quirin, J. Goodfellow *et al.*, Phys. Rev. Lett. **108**, 087601 (2012).
[11] M. Liu, A. J. Sternbach, and D. N. Basov, Rep. Prog. Phys. **80**, 014501 (2017).
[12] M. Matsubara, S. Manz, M. Mochizuki, T. Kubacka, A. Iyama, N. Aliouane, T. Kimura, S. L. Johnson, D. Meier, and M. Fiebig, Science **348**, 1112 (2015).
[13] C. T. Nelson, P. Gao, J. R. Jokisaari, C. Heikes, C. Adamo, A. Melville, S.-H. Baek, C. M. Folkman, B. Winchester, Y. Gu *et al.*, Science **334**, 968 (2011).
[14] S. O. Hruszkewycz, M. J. Highland, M. V. Holt, D. Kim, C. M. Folkman, C. Thompson, A. Tripathi, G. B. Stephenson, S. Hong, and P. H. Fuoss, Phys. Rev. Lett. **110**, 177601 (2013).
[15] P. Gao, J. Britson, C. T. Nelson, J. R. Jokisaari, C. Duan, M. Trassin, S.-H. Baek, H. Guo, L. Li, Y. Wang *et al.*, Nat. Commun. **5**, 3801 (2014).
[16] T. T. A. Lummen, Y. Gu, J. Wang, S. Lei, F. Xue, A. Kumar, A. T. Barnes, E. Barnes, S. Denev, A. Belianinov *et al.*, Nat. Commun. **5**, 3172 (2014).
[17] A. Grigoriev, R. J. Sichel, J. Y. Jo, S. Choudhury, L.-Q. Chen, H. N. Lee, E. C. Landahl, B. W. Adams, E. M. Dufresne, and P. G. Evans, Phys. Rev. B **80**, 014110 (2009).
[18] P. Chen, M. P. Cosgriff, Q. Zhang, S. J. Callori, B. W. Adams, E. M. Dufresne, M. Dawber, and P. G. Evans, Phys. Rev. Lett. **110**, 047601 (2013).
[19] F.-T. Huang and S.-W. Cheong, Nat. Rev. **2**, 17004 (2017).
[20] X. Wu, U. Petralanda, L. Zheng, Y. Ren, R. Hu, S.-W. Cheong, S. Artyukhin, and K. Lai, Sci. Adv. **3**, e1602371 (2017).
[21] D. Issenmann, S. Schleef, S. Ibrahimkutty, G. Buth, T. Baumbach, A. Plech, M. Beyer, and J. Demsar, Acta Phys. Pol. A **121**, 319 (2012).
[22] K. Istomin, V. Kotaidis, A. Plech, and Q. Kong, Appl. Phys. Lett. **90**, 022905 (2007).
[23] Y.-H. Kuo, S. Nah, K. He, T. Hu, and A. M. Lindenberg, J. Mater. Chem. C **5**, 1522 (2017).
[24] F. Chen, Y. Zhu, S. Liu, Y. Qi, H. Y. Hwang, N. C. Brandt, J. Lu, F. Quirin, H. Enquist, P. Zalden *et al.*, Phys. Rev. B **94**, 180104 (2016).
[25] J. Y. Jo, P. Chen, R. J. Sichel, S. J. Callori, J. Sinsheimer, E. M. Dufresne, M. Dawber, and P. G. Evans, Phys. Rev. Lett. **107**, 055501 (2011).
[26] A. Grigoriev, D.-H. Do, D. M. Kim, C.-B. Eom, B. Adams, E. M. Dufresne, and P. G. Evans, Phys. Rev. Lett. **96**, 187601 (2006).
[27] A. Grigoriev, D.-H. Do, D. M. Kim, C.-B. Eom, P. G. Evans, B. W. Adams, and E. M. Dufresne, Integr. Ferroelectr. **85**, 165 (2006).
[28] Y. Zhu, Z. Cai, P. Chen, Q. Zhang, M. J. Highland, I. W. Jung, D. A. Walko, E. M. Dufresne, J. Jeong, M. G. Samant *et al.*, Sci. Rep. **6**, 21999 (2016).
[29] G. Catalan, J. Seidel, R. Ramesh, and J. F. Scott, Rev. Mod. Phys. **84**, 119 (2012).
[30] A. von Hippel, R. G. Breckenridge, F. G. Chesley, and L. Tisza, Ind. Eng. Chem. **38**, 1097 (1946).
[31] B. Wul and J. M. Goldman, C.R. (Dokl.) Acad. Sci. URSS **51**, 21 (1946).

[32] G. H. Kwei, A. C. Lawson, S. J. L. Billinge, and S. W. Cheong, J. Phys. Chem. **97**, 2368 (1993).
[33] See Supplemental Material at http://link.aps.org/supplemental/10.1103/PhysRevLett.120.096101, which includes Refs. [34–42], for information on the experimental details, linear and nonlinear absorption, position dependence of ultrafast lattice responses, details of dynamical phase-field modeling, and second harmonic generation experiments.
[34] Advanced Photon Source, Compute x-ray absorption, http://11bm.xray.aps.anl.gov/absorb/absorb.php.
[35] T. F. Boggess, J. O. White, and G. C. Valley, J. Opt. Soc. Am. B **7**, 2255 (1990).
[36] R. A. Ganeev, M. Suzuki, M. Baba, M. Ichihara, and H. Kuroda, J. Opt. Soc. Am. B **25**, 325 (2008).
[37] W. F. Zhang, Y. B. Huang, M. S. Zhang, and Z. G. Liu, Appl. Phys. Lett. **76**, 1003 (2000).
[38] Y. L. Li, L. E. Cross, and L. Q. Chen, J. Appl. Phys. **98**, 064101 (2005).
[39] N. Bloembergen and P. S. Pershan, Phys. Rev. **128**, 606 (1962).
[40] G. Rupprecht and R. O. Bell, Phys. Rev. **135**, A748 (1964).
[41] M. Gorev, V. Bondarev, I. Flerov, M. Maglione, A. Simon, P. Sciau, M. Boulos, and S. Guillemet-Fritsch, J. Phys. Condens. Matter **21**, 075902 (2009).
[42] T. Yamada, J. Appl. Phys. **43**, 328 (1972).
[43] *Landolt-Börnstein, New Series III/1 Crystal and Solid State Physics: Elastic, Piezoelectric, Piezooptic and Electrooptic Constants of Crystals*, edited by K.-H. Hellwege, R. Bechmann, and R. F. S. Hearmon (Springer, New York, 1966).
[44] The *c*-lattice spacing of $BaTiO_3$ decreases with increasing temperature because of the tetragonal distortion accompanied by ferroelectric phase transition above room temperature [43].
[45] S. Liu, J. Xu, D. Guzun, G. Salamo, C. Chen, Y. Lin, and M. Xiao, Appl. Phys. B **82**, 443 (2006).
[46] A. K. Bandyopadhyay, P. C. Ray, and V. Gopalan, J. Phys. Condens. Matter **18**, 4093 (2006).
[47] A. K. Bandyopadhyay, P. C. Ray, L. Vu-Quoc, and A. R. McGurn, Phys. Rev. B **81**, 064104 (2010).
[48] Y. L. Li, S. Y. Hu, Z. K. Liu, and L. Q. Chen, Appl. Phys. Lett. **78**, 3878 (2001).
[49] Y. L. Li, S. Y. Hu, Z. K. Liu, and L. Q. Chen, Appl. Phys. Lett. **81**, 427 (2002).
[50] H. Motegi, J. Phys. Soc. Jpn. **32**, 202 (1972).
[51] E. Fatuzzo and W. J. Merz, J. Appl. Phys. **32**, 1685 (1961).
[52] R. E. Nettleton, J. Appl. Phys. **38**, 2775 (1967).
[53] W. J. Merz, J. Appl. Phys. **27**, 938 (1956).
[54] W. Känzig, Phys. Rev. **98**, 549 (1955).
[55] A. G. Chynoweth, Phys. Rev. **102**, 705 (1956).
[56] F. Rubio-Marcos, A. Del Campo, P. Marchet, and J. F. Fernández, Nat. Commun. **6**, 6594 (2015).
[57] J. Miao, T. Ishikawa, I. K. Robinson, and M. M. Murnane, Science **348**, 530 (2015).